Contents lists available at ScienceDirect

Optics Communications

CrossMark

Adaptive denoising method for Fourier ptychographic microscopy

Yao Fan [a,b,c], Jiasong Sun [a,b,c], Qian Chen [a,b], Mingqun Wang [a,b,c], Chao Zuo [a,b,c,*]

[a] School of Electronic and Optical Engineering, Nanjing University of Science and Technology, No.200 Xiaolingwei Street, Jiangsu Province 210094, China
[b] Jiangsu Key Laboratory of Spectral Imaging & Intelligent Sense, Nanjing, Jiangsu Province 210094, China
[c] Smart Computational Imaging Laboratory(SCIlab), Nanjing University of Science and Technology, Nanjing, Jiangsu Province 210094, China

A B S T R A C T

Fourier ptychographic microscopy (FPM) is a recently developed wide-field and high-resolution (HR) imaging technique, reconstructing HR spectrum from a series of low-resolution (LR) images at different illumination angles. Although many significant progresses have been made in FPM in the past few years, imaging noise is still an inevitable problem, which could seriously distort the results recovered using the conventional Fourier ptychography approach without image preprocessing. Generally, before FPM reconstruction, a thresholding denoising method is usually employed to eliminate the noise. However, conventional thresholding denoising algorithms cannot differentiate useful signals from imaging noise effectively, thus these algorithms usually eliminate signals and noise simultaneously. Here we propose an adaptive denoising method for FPM, which takes advantage of the information redundancy in FPM to separate signal from noise during the recovery process without any pre-knowledge about the noise statistics. Simulation and experimental results are presented to evaluate the performance of the proposed method. It is demonstrated that this method can both improve the accuracy and robustness of FPM and relax the imaging performance requirement for implementing high-quality FPM reconstruction.

© 2017 Elsevier B.V. All rights reserved.

1. Introduction

Fourier ptychographic microscopy (FPM) is a recently developed wide-field and high-resolution (HR) imaging technique [1], which utilizes angularly varying illumination and a phase retrieval algorithm to surpass the diffraction limit of the objective lens [2–8]. Similar to the conventional ptychography approaches [9,10], FPM shares its roots with phase retrieval algorithm [2–8] and synthetic aperture imaging [11–16]. In a typical FPM imaging system, a fixed-position LED matrix is used for angle-varied illuminations. At each illumination angle, a low-resolution (LR) intensity image of the specimen, with the resolution determined by the numerical aperture (NA) of the objective lens, is recorded. The recorded LR images from different illumination angles can be iteratively stitched in the Fourier domain to recover a HR complex image of the specimen. The final reconstruction resolution is determined by the sum of the NA of the objective lens and the largest incident angle of the LED matrix.

In order to improve the imaging performance of FPM, a series of improved algorithms have been proposed lately. Some of them improve the reconstruction accuracy and the recovery resolution of FPM [17–24], and others reduce measuring time of FPM imaging process and improve

data acquisition efficiency [21,25–29]. However, imaging noise is still an inevitable problem, which distorts high-frequency details and stains the background of the recovered image [30]. Although several of the methods described above, such as the Wirtinger flow optimization and the adaptive step-size [20,29], suppress the image noise from the final reconstruction results, they are achieved by means of improving the FPM convergence properties and not really eliminate noise in captured images. Take the example of the Wirtinger flow optimization algorithm, this method generally reside on expensive processing requirements, making it less appealing from a computational point of view.

Generally, better quality images not only improve the accuracy of FPM, but also improve its convergence speed. So, before FPM reconstruction, a thresholding denoising method is usually used to eliminate the noise in the initial data [21]. In the conventional thresholding denoising method, a fixed threshold for denoising is generally obtained by calculating the average intensity of the background of the dark-field image. However, the main drawback of this method is that it cannot differentiate useful signals and imaging noise effectively, thus these algorithms usually dislodge signal and noise simultaneously. Thus, there

---

* Corresponding author.
E-mail addresses: fanyaoscilab@163.com (Y. Fan), chenqian@njust.edu.cn (Q. Chen), surpasszuo@163.com (C. Zuo).

is a trade-off between the resolution of the HR image and the denoising effect in FPM.

As reported in [28], a key aspect of a successful FPM reconstruction is the data redundancy requirement of the recovery process. Precisely, such a data redundancy requirement is very important for recovering the lost phase information of the specimen. At least 35% aperture overlapping percentage in the Fourier domain is required for an accurate reconstruction of both intensity and phase information in FPM. Moreover, the FPM reconstruction result will not change significantly when the percentage of empty pixels in the image is less than aperture overlapping percentage in the Fourier domain. Based on the above considerations, we propose an adaptive denoising method for FPM, which takes advantage of the data redundancy in FPM. Different from the conventional thresholding denoising method, the adaptive denoising method introduces a difference matrix to separate signal from noise during the recovery process without any pre-knowledge about the noise statistics. In addition, we investigate the characteristic of the difference matrix to implement the adaptive updating of the denoising method. Simulation and experimental results are presented to evaluate the performance of the proposed adaptive denoising method and it is demonstrated that this method can both improve the accuracy and robustness of FPM and relax the imaging performance requirement for implementing high-quality FPM reconstruction.

2. Principle of FPM and adaptive denoising method

2.1. Principle of FPM

Before introducing the principle of the adaptive denoising method, it is worthwhile to review the basic concepts of FPM. As detailed in [1], a typical FPM platform consists of a LED matrix and a conventional microscopy with a low NA objective lens. We sequentially turn on single LED element in the matrix to illuminate the 2-D thin specimen from different angles and capture the corresponding LR intensity image. Since the 2-D thin specimen is illuminated by plane waves with different angles, the spectrum of the specimen on the back focal plane of the objective lens is shifted to the corresponding different positions. Thus, some of the frequency components that are beyond the NA of the objective lens are shifted into that is within the objective lens NA, so that they can be transferred to the sensor plane for recording. Then, these captured LR images are sequentially iterated in the Fourier domain to update the spectral information in the corresponding sub-region. The adjacent sub-regions overlap with each other, which extends the space-bandwidth product (SBP) and restores high-frequency information that exceeds the spatial resolution of the objective lens. Eventually, the HR intensity and phase image of the specimen are reconstructed simultaneously.

There are five steps in the reconstruction process of traditional FPM technology. First, initialize the HR complex amplitude distribution U_0 with amplitude of the LR image corresponding to the vertically incident plane wave. This HR complex amplitude distribution is used to generate multiple LR target images corresponding to different illumination angles. Second, the spectral information in a certain sub-aperture of the initial HR spectrum U_0 is intercepted to produce a LR complex amplitude distribution, which is called the target complex amplitude distribution $\sqrt{I_{mt}}e^{i\varphi_{mt}}$ (m represents the serial number of the captured images). Third, maintain the phase of the target complex amplitude image unchanged and update the amplitude portion $\sqrt{I_{mt}}$ of the target complex amplitude image $\sqrt{I_{mt}}e^{i\varphi_{mt}}$ with the actual measurement $\sqrt{I_{mc}}$ at the corresponding illumination angle, and finally we will get the updated complex amplitude distribution $\sqrt{I_{mc}}e^{i\varphi_{mt}}$. Fourth, the spectrum $u_m(k_{mx}, k_{my})$ of the updated target complex amplitude image $\sqrt{I_{mc}}e^{i\varphi_{mt}}$ is obtained by using the Fourier transform, which is used for updating the spectral components within the corresponding sub-aperture of the HR spectrum. Fifth, this replace-and-update sequence is repeated for all incident angles, and the fifth step is iterated several times until the solution converges.

In traditional FPM iteration process, the captured LR images are directly denoised using a fixed threshold. This fixed threshold is generally obtained by calculating the average intensity of the background in the dark-field image. However, an unavoidable problem in this denoising method is that it cannot distinguish noise from useful signals. This problem is very noticeable in the denoising of the dark-field image, because a large number of useful signals are usually weaker than the noise in dark-field image, and this means that these useful signals will be eliminated easily by using a fixed threshold denoising method. Fig. 1 shows the denoising results for a dark-field image with different denoising methods. As shown in Fig. 1(c), after using the conventional fixed threshold denoising for the dark-field image, the noise of the dark-field image is eliminated, but a large number of effective signals are also eliminated. Eventually, such a loss of information will result in the lack of details of the FPM reconstructed HR image.

2.2. Adaptive denoising method

In order to effectively eliminate the noise in captured images, a noise discrimination factor is introduced to the third step of the above process to differentiate useful signals and noise approximately, which is expressed as $C_m = \sqrt{I_{mc}} - \sqrt{I_{mt}}$. It can be seen that the updated image distribution $\sqrt{I_{mc}}e^{i\varphi_{mt}}$ can also be expressed as $(C_m + \sqrt{I_{mt}})e^{i\varphi_{mt}}$. It is not difficult to find that C_m is a matrix which has the same size as the captured image, and its values represent the difference between actual amplitude $\sqrt{I_{mc}}$ and the amplitude portion $\sqrt{I_{mt}}$ of the target complex amplitude image $\sqrt{I_{mc}}e^{i\varphi_{mt}}$ at the identical illumination angle. In the ideal noiseless case, the values of the C_m matrix mainly concentrate within a small vicinity around 0. Conversely, with the noise increasing in captured images, the values of the C_m matrix depart from 0 gradually. Based on these premises, the matrix C_m can be used to differentiate useful signals from noise pixel by pixel approximately. Specifically, if the value of a pixel in matrix C_m is almost close to 0, it indicates that the pixel tend to be noise. On the other hand, if the value of a pixel of matrix C_m is far away from 0, it means that the pixel is more likely to be noise.

Based on the above knowledge, the adaptive denoising process of images can be seen as making the value of the C_m matrix as close as possible to the ideal noise-free situation. The process of FPM reconstruction using the adaptive method is shown in Fig. 2. First, similar to the traditional FPM refactoring, it starts with a HR complex amplitude distribution of the specimen profile: U_0. Second, produce target complex amplitude distribution $\sqrt{I_{mt}}e^{i\varphi_{mt}}$. Third, solve the difference matrix $C_m = \sqrt{I_{mc}} - \sqrt{I_{mt}}$ to differentiate noise from useful image signals, and update the values of the matrix by setting the value of the C_m matrix which is far away from 0 to 0. The updated matrix $C_{m_{update}}$ is obtained as a denoising factor. Fourth, the denoising matrix $C_{m_{update}}$ is used to update the intensity components of the target images, while the phase components remain unchanged, the resulting complex amplitude distribution is $(C_{m_{update}} + \sqrt{I_{mt}})e^{i\varphi_{mt}}$. Fifth, the updated complex amplitude distribution is used to modify the corresponding spectral regions of the HR complex amplitude distribution U_0. Lastly, this replace-and-update sequence is repeated several times until the solution converges. Fig. 1(d) shows the dark-field image using the adaptive denoising method. The image not only eliminates the noise, but also preserves more useful signals of the image compared with Fig. 1(c).

In the iterative process including adaptive denoising method, there is a step that needs to be discussed, that is, the initialization of the FPM iterative process. For FPM technology, it is common to use a LR bright-field image to initialize the HR spectrum, but as a phase retrieval algorithm, using a constant to initialize can also get the correct convergence results. In the adaptive denoising method, the selection of the initialization step can be discussed in different cases. In the first case, all LR images are captured for adaptive denoising. In this case, a LR bright-field image must be used to initialize, since this ensures that the obtained C_m matrix can distinguish between noise and useful signals. In
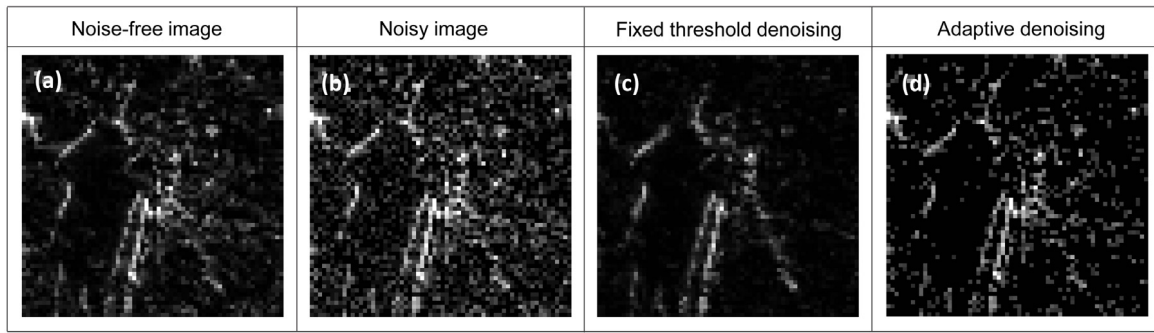
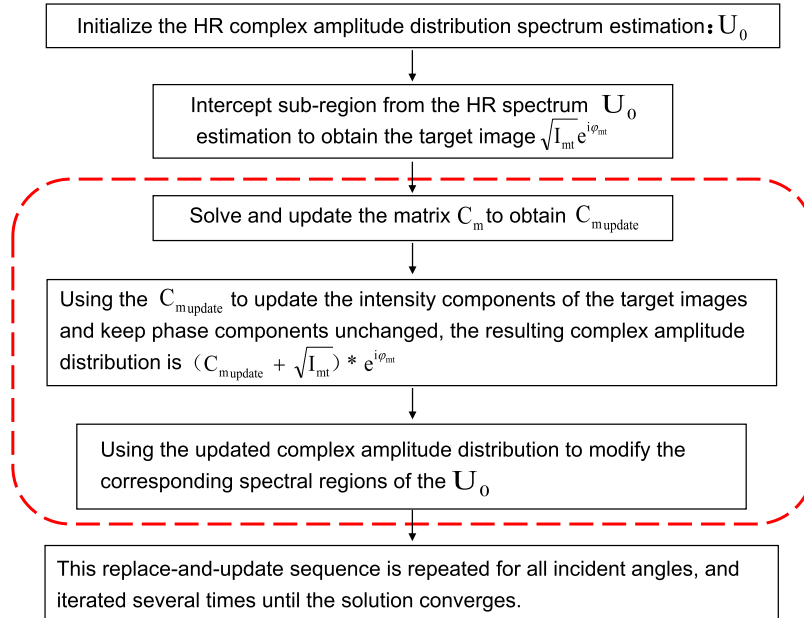**Fig. 1.** Denoising results with different denoising methods.

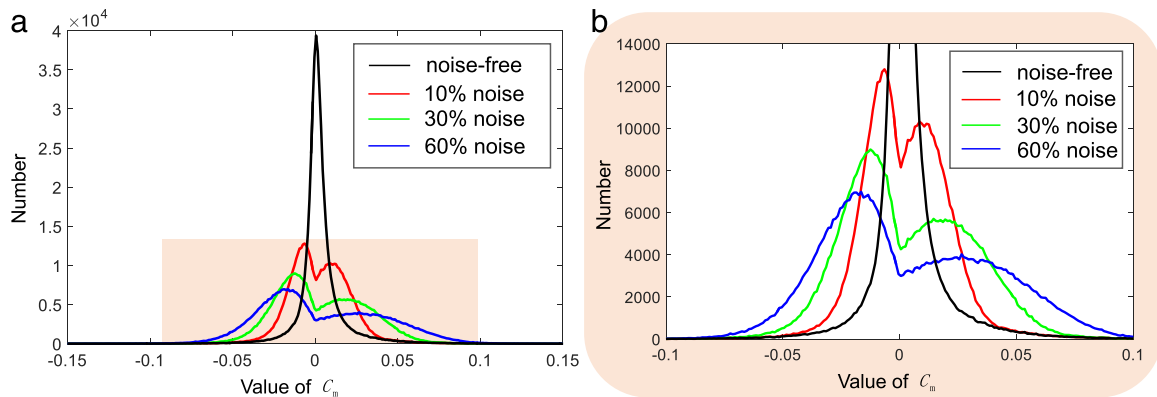**Fig. 2.** FPM reconstruction process including adaptive denoising method.

Fig. 3. C_m distribution curve of the image with different noise levels.

the second case, the adaptive denoising process is performed only on LR dark-field images. In this case, the same HR results can be obtained by initializing the HR spectrum using LR bright-field image and a constant. All of the simulations and experiments in this paper are performed in the second case.

In the adaptive denoising method, determining the update range of the matrix C_m is a critical step. In the C_m matrix, if the value of the pixel is far away from 0, it will be identified to be noise, so the value

of these pixels should not be iterated in the reconstruction process. Specifically, there are two so called denoising thresholds that need to be determined to eliminate the value of pixels that is far away from 0, and we propose a method to determine these two thresholds. In order to obtain the initial denoising thresholds, we investigate the C_m distribution curves of all images with different noise levels at the first iteration and display them with different colors in Fig. 3. It can be found that the values of C_m are concentrated near 0 when there is no noise,
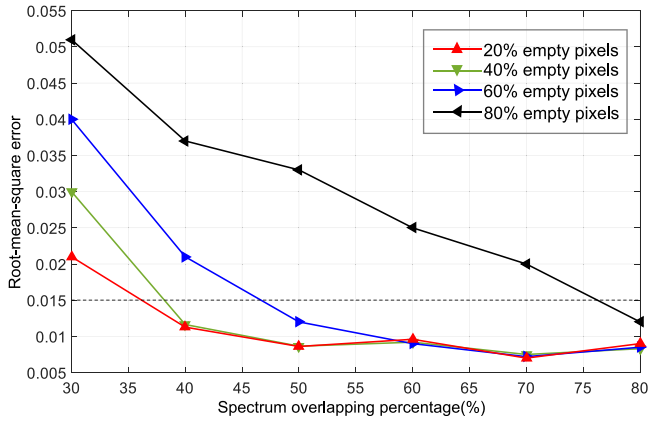
Fig. 4. RMSE curves for multiple empty pixel percentages under different spectrum overlapping percentage.
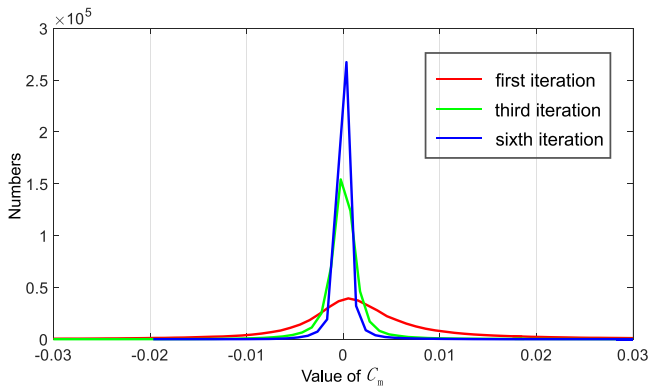

Fig. 5. C_m distribution curve under different iterations.

and there is only one maximum value of C_m curve in the vicinity of 0. Compared with the noise-free situation, the number of values near 0 in the C_m decline significantly and the number of values far from 0 increase

significantly with the addition of noise. In addition, with the levels of noise increasing, the values distribution of C_m matrix are more and more dispersed, and the C_m curve has two maximum values around 0.

According to the requirements of FPM data redundancy, at least 35% of the spectrum overlapping percentage is needed in FPM iterations [28]. On this basis, we further study the relationship between spectrum overlapping percentage and empty pixel percentage. Fig. 4 shows the Root-mean-square error ($RMSE$) curves of FPM reconstructed results for multiple empty pixel percentages under different spectrum overlapping percentage. It can be found that with the spectrum overlapping percentage increasing, the curves gradually converge to a stable small value, and the convergence critical point has a linear relationship with the empty pixel percentage. In other words, the reconstructed result of FPM is not significantly affected when the empty pixel percentage is smaller than the spectrum overlapping percentage.

Based on the considerations above, we introduce a percentage P_b to achieve the adaptive update of the denoising threshold. The spectrum overlapping percentage P_a is calculated according to the system parameters, as

$$P_a = \begin{cases} \frac{1}{\pi}\left[2\arccos\left(\frac{1}{2R_{LED}}\right) - \frac{1}{R_{LED}}\sqrt{1 - \left(\frac{1}{2R_{LED}}\right)^2} \right], & R_{LED} > \frac{1}{2} \\ 0 & else \end{cases} \tag{1}$$

and

$$R_{LED} = NA\frac{\sqrt{\left(D_{LED}\right)^2 + h^2}}{D_{LED}}. \tag{2}$$

In these equations, D_{LED} denotes the distance between adjacent LED elements and h is the distance (at the z direction) between the LED matrix and specimen. Given percentage P_b greater than $(1 - P_a)$, and the threshold of the update difference matrix in the interval $[-T, T]$ to guarantee the percentage of the number of values in this interval to the total number of values in the C_m matrix is around P_b. Table 1 provides the corresponding value of P_a and P_b. So we can determine the appropriate P_b value based on this table in the simulation and experiment.

In order to explore whether the adaptive threshold updating method applies to different iterations of FPM reconstruction, we investigate
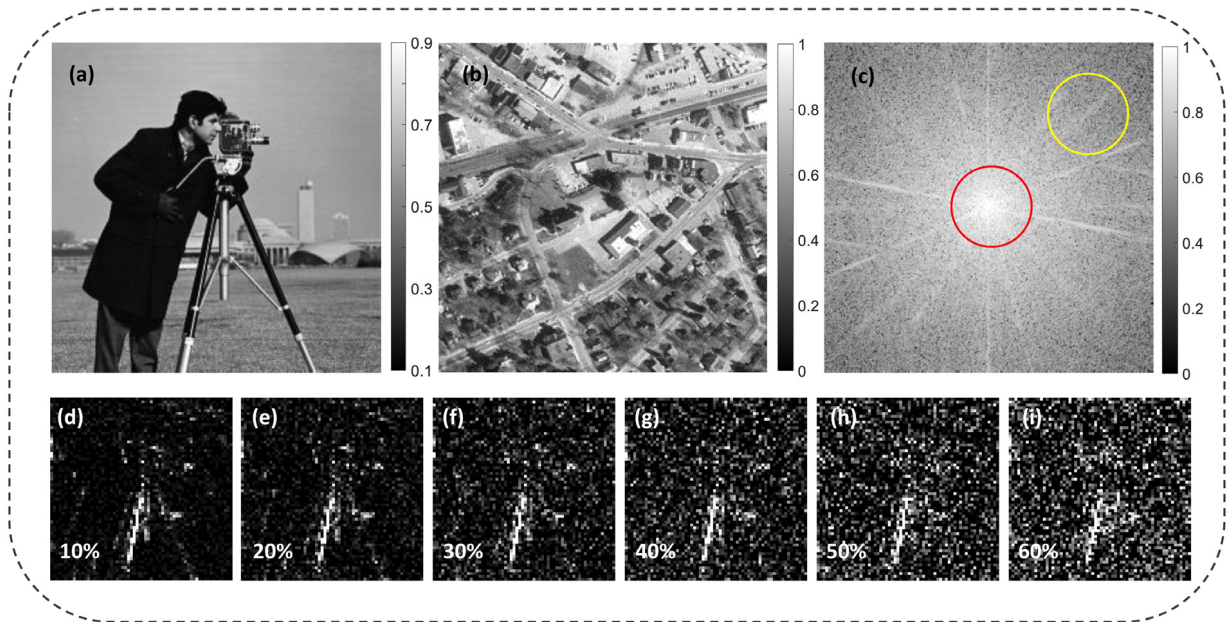

Fig. 6. Input intensity and phase image for FPM reconstruction. (a) Intensity; (b) Phase; (c) Fourier spectrum; the red and yellow circles indicate the captured sub-spectrums under orthogonal and oblique illuminations; (d)–(i) low-resolution raw images with different levels of Gaussian noise. (For interpretation of the references to color in this figure legend, the reader is referred to the web version of this article.)
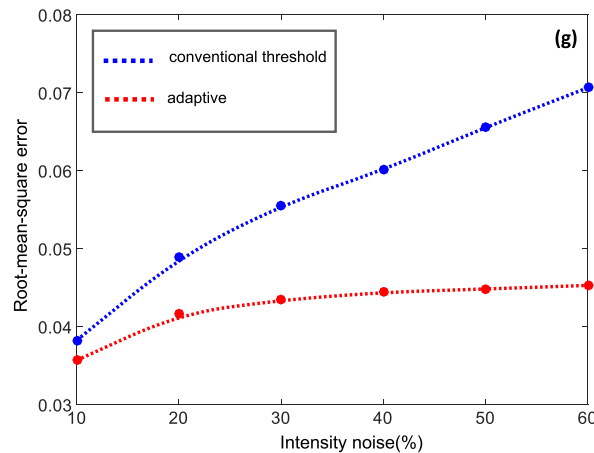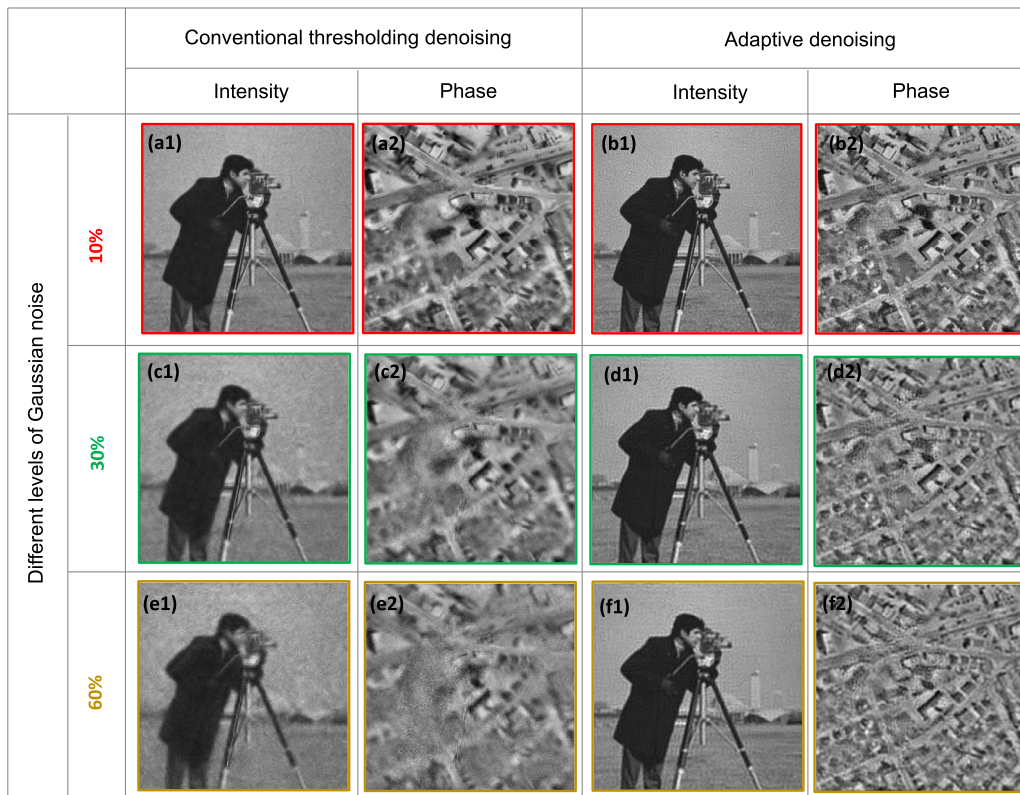
Fig. 7. FPM reconstruction results with different denoising methods for Gaussian noise.

the distribution curves of C_m matrix at different iterations shown in Fig. 5. With the number of iterations increasing, it can be seen that the curves converge gradually and the values of the C_m matrix approach 0. Therefore, when there is noise, the interval of $[-T, T]$ determined by the percentage P_b is as far as possible to eliminate the values far from 0 while keeping the values in the C_m matrix near 0.

3. Simulation

To verify the effectiveness of the adaptive denoising method, the same image is processed under the same parameters using the adaptive denoising method and the conventional thresholding denoising method. The parameters in the simulations are chosen to realistically model a light microscopy, with an incident wavelength of 526 nm, an imaging pixel size of 2.62 μm, a small segment of 64×64 pixels and an objective NA of 0.1 (4x). In simulation, a 11×11 LED matrix is used to illuminate the specimen with different incident angles. The LED matrix is placed 75 mm below the specimen, and the distance between adjacent LED

Table 1
The corresponding value of P_a and P_b.

P_a	40%–50%	50%–60%	60%–70%	70%–80%
P_b	>50%	>40%	>30%	>20%

elements is 4 mm. A set of 121 LR intensity images are simulated. In these parameters setting, the spectrum overlapping percentage P_a of the FPM iteration is 66.5%, so we set the value of P_b in the simulation to 60% based on the proposed strategy. In order to exclude the effects of iterative steps, we maintain the value of the iterative step-size to 0.5. All simulations have been run for 10 iterations.

3.1. Simulation of Gaussian noise

The HR input intensity and phase profiles are shown in Fig. 6(a) and (b), which serve as the ground truth for the simulated complex object. Besides the idealized situation, each LR image is corrupted with
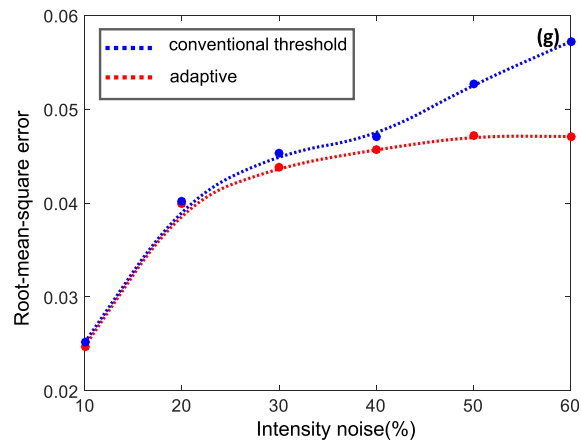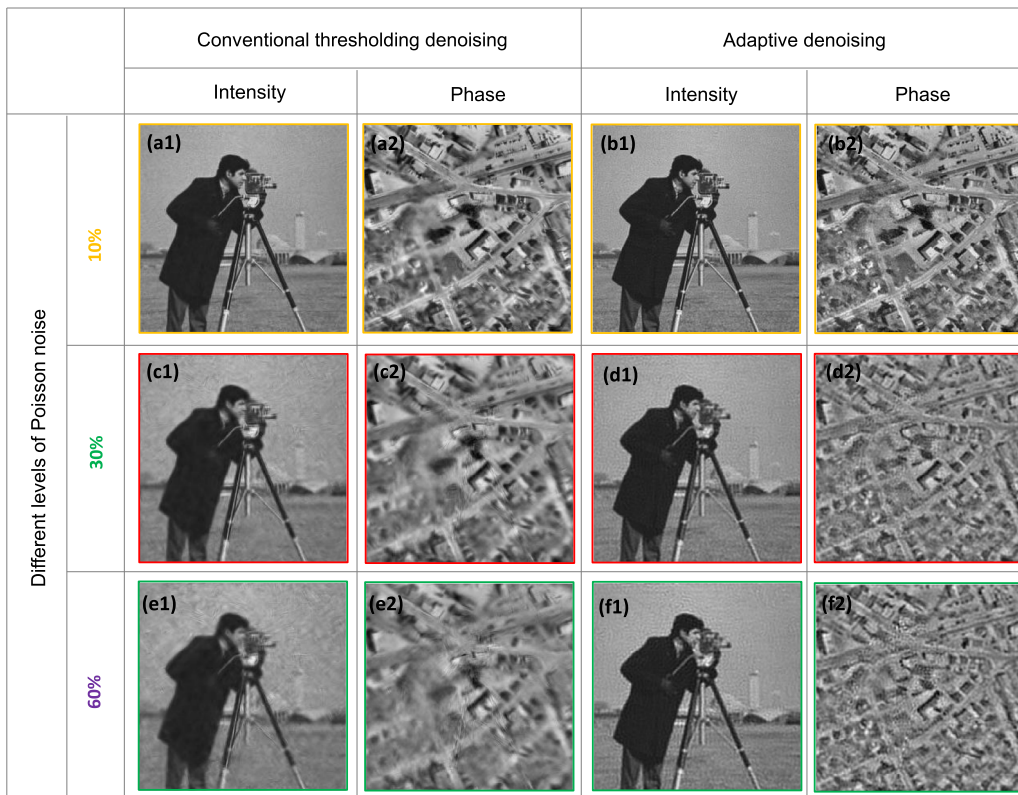
Fig. 8. FPM reconstruction results with different denoising methods for Poisson noise.

Gaussian noise in different variances. Since the signal power of dark-field images from large-angle illuminations is much weaker than that of the bright-field images, they suffer more from the noise, which is in accord with the actual experimental conditions. To illustrate the level of noise more intuitively, six typical noisy dark-field intensity images are given in Fig. 6(d)–(i). The noise level is quantified by the average mean absolute error ($AMAE$) [29], defined as $AMAE = \langle |I_n - I| \rangle / \langle I \rangle$, where $\langle I \rangle$ is the mean value of noise-free dark-field intensity images and $\langle |I_n - I| \rangle$ is the mean absolute error of the corresponding noisy images.

The conventional thresholding denoising method and adaptive denoising method are simulated with images containing six different levels of noise. In conventional thresholding denoising method, the threshold is usually set to the average background intensity of the dark-field image with the largest illumination angle. Fig. 7(a), (c) and (e) show the reconstructed results of intensity and phase using the conventional thresholding denoising method. With the noise increasing, the reconstructed intensity images become worse and phase images are gradually blurred. As a comparison, reconstruction results using

adaptive denoised images are shown in Fig. 7(b), (d) and (f). We can see that the quality of reconstructed results using adaptive denoising methods is always better than that using conventional thresholding denoising method. We also quantify reconstruction accuracy of adaptive denoising method using the $RMSE$ metric in Fig. 7(g). It is shown that, FPM algorithm with adaptive denoising method is able to recover a high-quality HR result.

3.2. Simulation of Poisson noise

Similar to the simulation of Gaussian noise, we corrupt LR images with different levels of Poisson noise. The reconstructed results for different levels of Poisson's noise are shown in Fig. 8. As can be seen, with the level of Poisson noise increasing, the denoising effect of conventional thresholding denoising method is deteriorated. As a comparison, the reconstructed results of the adaptive denoising method are shown in Fig. 8(b), (d) and (f). We also quantify the FPM reconstruction qualities using the $RMSE$ metric in Fig. 8(g). As is shown in Fig. 8, we can easily
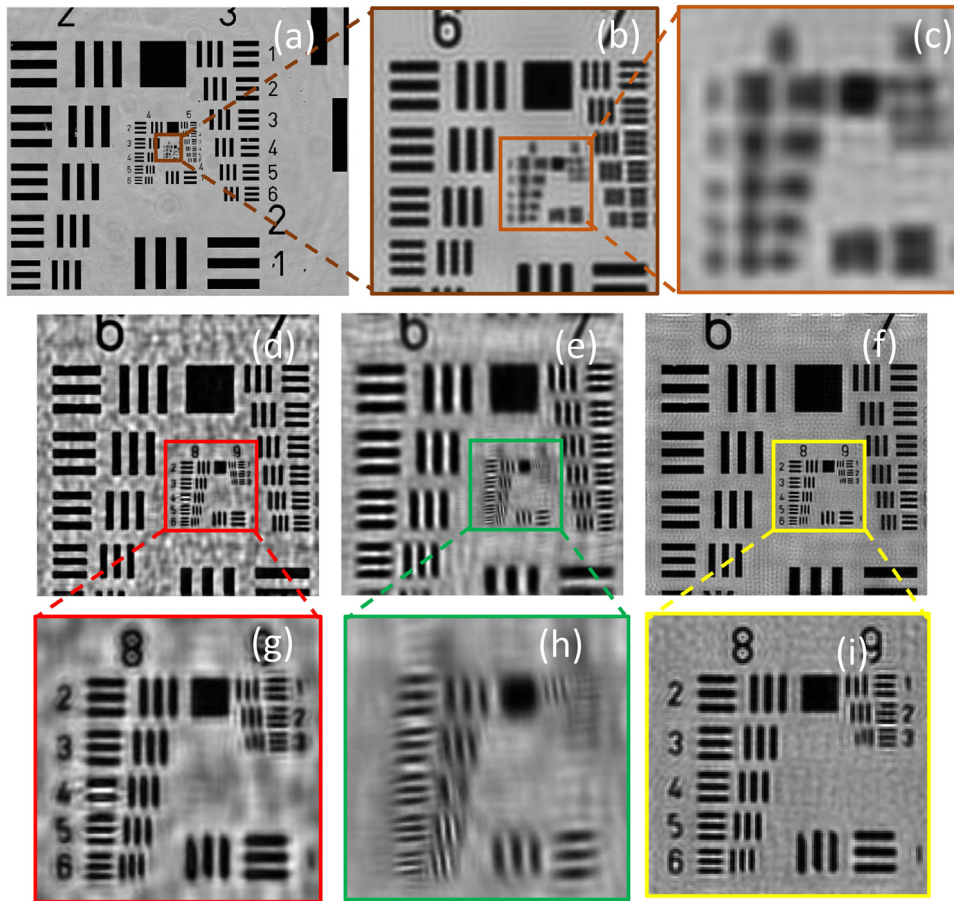
Fig. 9. Experimental results of a USAF target. (a) The low-resolution full-field image. (b–c) The corresponding region of interest. (d–i) The comparison of reconstructed intensity of image data under three ways.

find that adaptive denoising method can effectively eliminate noise and therefore improve the quality of FPM reconstructed result.

4. Experiments

In order to evaluate the effectiveness of the adaptive denoising method experimentally, we compare the recovered intensity distributions of one segment in a USAF target using conventional thresholding denoising method and the adaptive denoising method respectively.

We first utilize a light microscopy (OLYMPUS CX22, magnification 4x, NA = 0.1) as the imaging system and an LED matrix (21×21, incident wavelength À = 632 nm) as the light source for providing angle-varied illuminations. The distance between adjacent LED elements is 2.5 mm, and the LED matrix is placed at 87.5 mm below the objective table. A scientific CMOS camera (PCO.edge) with the pixel size of 6.5 μm is used for recording images under different incident angles. Under these experimental parameters, the spectrum overlapping percentage is 82%, so we set the value of P_b to 60%. A set of 441 LR intensity images are captured using this setup.

One of the captured LR full-field images is shown in Fig. 9(a). In this experiment, a sub-region of size of 128×128 is extracted to recover the HR image using the conventional thresholding denoising method and the adaptive denoising method respectively, and the sub-region is shown in Fig. 9(b). Fig. 9(d)–(f) show the results of FPM reconstruction in the case of no denoising, conventional thresholding denoising and adaptive denoising. The HR result from the images without denoising is shown in Fig. 9(d). We can see that strong artifacts are superimposed on the final reconstruction result, which not only smear the background but also distort several small-scale features. In the conventional thresholding denoising method, we capture the dark-field

image of the largest illumination angle without placing any specimens, and the average intensity of this dark-field image is used as a threshold to eliminate noise. Fig. 9(e) and (h) show HR results, which background becomes cleaner, but image become seriously blurred due to the massive loss of image details. This result indicate an improper choice of threshold can lead to blurring in high-frequency details if the threshold is too large or sub-optimal removal of noise artifacts if the threshold chosen is too small. The reconstructed results of the adaptive denoising method are shown in Fig. 9(f) and (i). It can be seen that the noise is eliminated while preserving the useful signals to the greatest extent possible, resulting in a better reconstructed image with a uniform background and all groups of features clearly resolved.

In addition, the proposed adaptive denoising method is tested on human blood smear. The experimental parameters are chosen to realistically model an FPM platform, with an incident illumination wavelength of 632 nm, 530 nm and 450 nm, an image sensor with pixel size of 3.75 μm (The imaging source), and an 4X objective with NA of 0.16 (OLYMPUS UPlanSApo). We experiment the use of the central 9×9 LEDs in the matrix placed 75 mm below the specimen, and the distance between adjacent LEDs is 4 mm. In this experimental system, the spectrum overlapping percentage is 80%, so we set the value of P_b in the experiment to 60%. Fig. 10(a) presents the full-filed of the specimen and Fig. 10(b) and (c) show the corresponding magnified area of interest. Fig. 10(d) and (e) show the reconstructed results of the image processed using the conventional thresholding denoising method. As can be seen in Fig. 10(e), the background of the reconstructed HR result is contaminated and the quality of image is bad. And the HR images shown in Fig. 10(f) and (g) suggest that adaptive denoising method brings clear detail of the cell and clean background. It is illustrated that the adaptive denoising method can eliminate the noise more effectively and improve the quality of the FPM reconstructed HR image significantly.
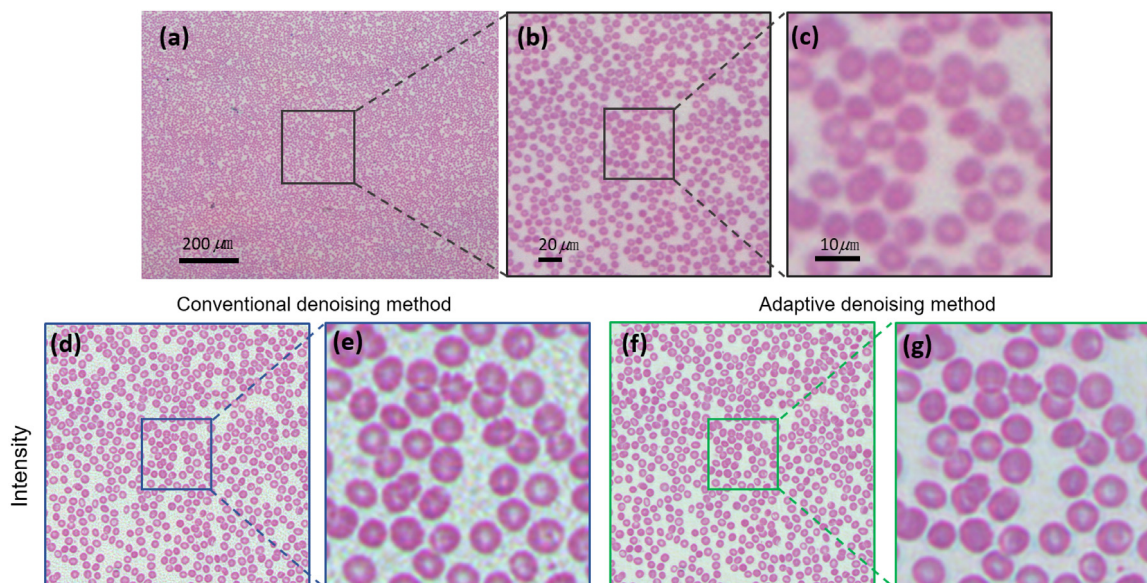
Fig. 10. Experimental results of Human blood smear. (a) The full-field image. (b) Region of interest for reconstruction. (c–e) The comparison of reconstructed intensity of image data under three ways.

5. Conclusion

In order to solve the problem of noise, this paper explores the characteristics of image signals and noise in FPM algorithm and introduces a difference matrix as noise discrimination factor for separating noise and signals. Briefly speaking, in the ideal noiseless case, the values of the difference matrix mainly concentrate within a small vicinity around 0. Conversely, with the noise increasing, the value of the difference matrix depart from 0 gradually. According this difference matrix, we differentiate the noise from useful signals pixel by pixel to provide a strong basis for the subsequent denoising process. In the process of eliminating noise, taking advantage of the data redundancy in FPM, we investigate the quality of HR results of different empty pixel percentage under different spectrum overlapping percentage and propose a method to adaptively determine the denoising threshold. It is demonstrated that the proposed adaptive denoising method can more effectively eliminate noise and preserve more effective signals compared to the conventional thresholding denoising method of selecting a fixed threshold for all captured images to denoise. The reported adaptive denoising method not only improve the accuracy and robustness of FPM , but also relax the imaging performance requirement for implementing high-quality FPM reconstruction.

The adaptive denoising method improves the reconstruction quality of FPM from the aspect of image denoising. However, there are several methods which can suppress the noise and improve the reconstruction quality from other aspects such as iterative optimization frame-work and adaptive step-size [20,29]. In essence, the adaptive denoising method does not conflict with these methods, it can be safely predicted that the combination of our adaptive denoising method and those developed FPM methods could further improve the reconstruction quality of FPM.

Acknowledgment

References

[1] G. Zheng, R. Horstmeyer, C. Yang, Wide-field, high-resolution Fourier ptychographic microscopy, Nature Photonics 7 (9) (2013) 739–745.

[2] R.A. Gonsalves, Phase retrieval and diversity in adaptive optics, Opt. Eng. 21 (5) (1982) 215829.

[3] J.R. Fienup, Phase-retrieval algorithms for a complicated optical system, Appl. Opt. 32 (10) (1993) 1737–1746.

[4] L. Allen, M. Oxley, Phase retrieval from series of images obtained by defocus variation, Opt. Commun. 199 (1) (2001) 65–75.

[5] B.H. Dean, C.W. Bowers, Diversity selection for phase-diverse phase retrieval, J. Opt. Soc. Amer. A 20 (8) (2003) 1490–1504.

[6] H. Faulkner, J. Rodenburg, Movable aperture lensless transmission microscopy: a novel phase retrieval algorithm, Phys. Rev. Lett. 93 (2) (2004) 023903.

[7] P. Bao, F. Zhang, G. Pedrini, W. Osten, Phase retrieval using multiple illumination wavelengths, Opt. Lett. 33 (4) (2008) 309–311.

[8] M. Guizar-Sicairos, J.R. Fienup, Phase retrieval with transverse translation diversity: a nonlinear optimization approach, Opt. Express 16 (10) (2008) 7264–7278.

[9] P. Thibault, M. Dierolf, O. Bunk, A. Menzel, F. Pfeiffer, Probe retrieval in ptychographic coherent diffractive imaging, Ultramicroscopy 109 (4) (2009) 338–343.

[10] A.M. Maiden, J.M. Rodenburg, An improved ptychographical phase retrieval algorithm for diffractive imaging, Ultramicroscopy 109 (10) (2009) 1256–1262.

[11] C.J. Schwarz, Y. Kuznetsova, S. Brueck, Imaging interferometric microscopy, Opt. Lett. 28 (16) (2003) 1424–1426.

[12] S.A. Alexandrov, T.R. Hillman, T. Gutzler, D.D. Sampson, Synthetic aperture Fourier holographic optical microscopy, Phys. Rev. Lett. 97 (16) (2006) 168102.

[13] V. Mico, Z. Zalevsky, P. García-Martínez, J. García, Synthetic aperture superresolution with multiple off-axis holograms, J. Opt. Soc. Amer. A 23 (12) (2006) 3162–3170.

[14] J. Di, J. Zhao, H. Jiang, P. Zhang, Q. Fan, W. Sun, High resolution digital holographic microscopy with a wide field of view based on a synthetic aperture technique and use of linear CCD scanning, Appl. Opt. 47 (30) (2008) 5654–5659.

[15] T. Gutzler, T.R. Hillman, S.A. Alexandrov, D.D. Sampson, Coherent aperture-synthesis, wide-field, high-resolution holographic microscopy of biological tissue, Opt. Lett. 35 (8) (2010) 1136–1138.

[16] A.E. Tippie, A. Kumar, J.R. Fienup, High-resolution synthetic-aperture digital holography with digital phase and pupil correction, Opt. Express 19 (13) (2011) 12027–12038.

[17] Z. Bian, S. Dong, G. Zheng, Adaptive system correction for robust Fourier ptychographic imaging, Opt. Express 21 (26) (2013) 32400–32410.

[18] J. Sun, Q. Chen, Y. Zhang, C. Zuo, Sampling criteria for Fourier ptychographic microscopy in object space and frequency space, Opt. Express 24 (14) (2016) 15765–15781.

[19] X. Ou, G. Zheng, C. Yang, Embedded pupil function recovery for Fourier ptychographic microscopy, Opt. Express 22 (5) (2014) 4960–4972.

[20] L. Bian, J. Suo, G. Zheng, K. Guo, F. Chen, Q. Dai, Fourier ptychographic reconstruction using Wirtinger flow optimization, Opt. Express 23 (4) (2015) 4856–4866.

[21] L. Tian, X. Li, K. Ramchandran, L. Waller, Multiplexed coded illumination for Fourier Ptychography with an LED array microscope, Biomed. Opt. Exp. 5 (7) (2014) 2376–2389.

[22] J. Sun, Q. Chen, Y. Zhang, C. Zuo, Efficient positional misalignment correction method for Fourier ptychographic microscopy, Biomed. Opt. Exp. 7 (4) (2016) 1336–1350.

[23] X. Ou, R. Horstmeyer, G. Zheng, C. Yang, High numerical aperture Fourier ptychography: principle, implementation and characterization, Opt. Express 23 (3) (2015) 3472–3491.

[24] J. Sun, C. Zuo, L. Zhang, Q. Chen, Resolution-enhanced fourier ptychographic microscopy based on high-numerical-aperture illuminations, Sci. Rep. 7 (1) (2017) 1187.

[25] L. Bian, J. Suo, G. Situ, G. Zheng, F. Chen, Q. Dai, Content adaptive illumination for Fourier ptychography, Opt. Lett. 39 (23) (2014) 6648–6651.

[26] S. Dong, R. Shiradkar, P. Nanda, G. Zheng, Spectral multiplexing and coherent-state decomposition in Fourier ptychographic imaging, Biomed. Opt. Exp. 5 (6) (2014) 1757–1767.

[27] J. Sun, Y. Zhang, C. Zuo, Q. Chen, S. Feng, Y. Hu, J. Zhang, Coded multi-angular illumination for Fourier ptychography based on Hadamard codes, in: International Conference on Optical and Photonic Engineering, IcOPEN2015, International Society for Optics and Photonics, 2015, p. 95242C.

[28] S. Dong, Z. Bian, R. Shiradkar, G. Zheng, Sparsely sampled Fourier ptychography, Opt. Express 22 (5) (2014) 5455–5464.

[29] C. Zuo, J. Sun, Q. Chen, Adaptive step-size strategy for noise-robust Fourier ptychographic microscopy, Opt. Express 24 (18) (2016) 20724–20744.

[30] L.-H. Yeh, J. Dong, J. Zhong, L. Tian, M. Chen, G. Tang, M. Soltanolkotabi, L. Waller, Experimental robustness of Fourier ptychography phase retrieval algorithms, Opt. Express 23 (26) (2015) 33214–33240.